High-resolution survey for planetary companions to young stars in the Taurus molecular cloud

Frantz Martinache, A Wallace, J Kammerer, M Ireland, C Federrath, A Kraus, S Maddison, A Rizzuto, E Birchall

Monthly Notices of the ROYAL ASTRONOMICAL SOCIETY

MNRAS **498,** 1382–1396 (2020) doi:10.1093/mnras/staa2434
Advance Access publication 2020 August 17

High-resolution survey for planetary companions to young stars in the Taurus molecular cloud

A. L. Wallace [1]★ J. Kammerer,[1,2] M. J. Ireland [1] C. Federrath,[1] A. L. Kraus,[3] S. T. Maddison,[4] A. Rizzuto,[3] E. K. Birchall [1] and F. Martinache [5]

[1]*Research School of Astronomy and Astrophysics, Australian National University, Canberra, ACT 2611, Australia*
[2]*European Southern Observatory, Karl-Schwarzschild-Str 2, D-85748 Garching, Germany*
[3]*Department of Astronomy, University of Texas, Austin, TX 78712, USA*
[4]*Centre for Astrophysics and Supercomputing, Swinburne University of Technology, Melbourne, VIC 3122, Australia*
[5]*Laboratoire Lagrange, Université Côte d'Azur, Observatoire de la Côte d'Azur, CNRS, Parc Valrose, Bât. H. FIZEAU, F-06108 Nice, France*

Accepted 2020 August 5. Received 2020 July 29; in original form 2020 April 14

ABSTRACT

Direct imaging in the infrared at the diffraction limit of large telescopes is a unique probe of the properties of young planetary systems. We survey 55 single class I and class II stars in Taurus in the *L*' filter using natural and laser guide star adaptive optics and the near-infrared camera (NIRC2) of the Keck II telescope, in order to search for planetary-mass companions. We use both reference star differential imaging and kernel phase techniques, achieving typical 5σ contrasts of ∼6 mag at separations of 0.2 arcsec and ∼8 mag beyond 0.5 arcsec. Although, we do not detect any new faint companions, we constrain the frequency of wide separation massive planets, such as HR 8799 analogues. We find that, assuming hot-start models and a planet distribution with power-law mass and semimajor axis indices of −0.5 and −1, respectively, less than 20 per cent of our target stars host planets with masses $>2\,M_{\rm J}$ at separations >10 au.

Key words: techniques: high angular resolution – planets and satellites: detection – planets and satellites: gaseous planets.

1 INTRODUCTION

Direct imaging of exoplanets is an important method to study planetary systems and gain insight into formation scenarios. Most directly imaged exoplanets have been found in young star systems when the planets are still hot and emit in the infrared (e.g. HR 8799; Marois et al. 2008), while some have been found in the process of formation (Keppler et al. 2018). Most directly imaged planets are at wide separations (>20 au) from their host stars but models of planet distributions (Fernandes et al. 2019) indicate that these systems are rare. Giant planets such as Jupiter are likely to form by core accretion that occurs closer to the star (∼5 au.)

The Taurus Molecular Cloud (TMC) is ideal for studying planet formation due to its relative proximity (∼140 pc) and numerous young stars (< 2 Myr) (Torres et al. 2009). Many of these young stars have prominent disc structures (ALMA Partnership 2015; Huang et al. 2020), which may be indicative of planet formation. A planet in the process of formation will radiate in the near-infrared. In an optically thick disc, the planet will be hidden at these wavelengths. However, a giant planet (∼0.5 $M_{\rm J}$ and above) is expected to clear a gap in the disc (Crida & Morbidelli 2007). Many of the discs in our sample have gaps present in their dust distribution, as indicated by ALMA surveys (Long et al. 2018) and, although their origin is still hotly debated, one possibility is giant planet formation.

The circumstellar discs in the TMC have been extensively studied over the years in terms of their mass (Andrews & Williams 2005; Andrews et al. 2013), structure, and distribution, as have the discs in other nearby star-forming regions such as Upper Scorpius and Ophiuchus (Carpenter, Ricci & Isella 2014; Van Der Plas et al. 2016; Kuruwita et al. 2018). Surveys have also been conducted to detect planets in these star-forming regions (Tanner et al. 2007; Metchev & Hillenbrand 2009) and some have found potentially planet-mass companions at wide separations (e.g. DH Tau b; Itoh et al. 2005) as well as a close companion to CI Tau using radial velocity (Johns-Krull et al. 2016). However, these surveys were unable to achieve the necessary sensitivity for planetary-mass companions on Solar system scales. Kraus et al. (2011) managed to detect new brown dwarf companions at small separations and achieved a mass sensitivity of ∼20 $M_{\rm J}$. In part of this earlier work, emission with total luminosity comparable to a forming planet was discovered around LkCa 15 (Kraus & Ireland 2011), although the complex transitional (or 'pre-transitional') nature of this disc has meant that a physically motivated radiative transfer model could not be made at the time. A scattering origin for the emission was, however, strongly suggested by further observations with Sphere and ZIMPOL (Thalmann et al. 2015).

The purpose of our study is to search for giant planets around young stars in the TMC still accreting from their discs, and determine dominant mechanisms for planet formation. This study is unique because, for the first time, we attempted to probe the inner regions of these systems in search of Solar system analogues, at a time where the significant presence of disc gas means that planetary luminosities would be highest. As the TMC is the nearest star-forming region of its size (Güdel et al. 2007) and the projected separation of any planets decreases with the distance, it is the most favourable region for resolving the peak of the giant planet distribution at physical separations of <10 au. Using planet distributions from Cumming et al. (2008) and later by Fernandes et al. (2019), it is clear that even

★ E-mail: alexander.wallace@anu.edu.au

at this close distance, the majority of planets are inside the ∼20–30 au limits of a typical coronagraph.

When planets form, they heat up and radiate in infrared wavelengths and are at their brightest during runaway accretion. After formation, the planets continue to radiate for some time and should still be self-luminous after millions of years as shown by the HR 8799 and β-Pictoris systems (Marois et al. 2008; Lagrange et al. 2010). The evolution of planet luminosity is an important factor in this work as it determines our detection capability. However, many details of the accretion luminosity remain uncertain. The luminosity of a circumplanetary disc is dependent on the accretion rate as well as the mass and radius of the planet, and whether and where the circumplanetary disc is truncated (Zhu 2015). The post-accretion luminosity of hot-start planets (i.e. planets that do not lose entropy in an accretion shock) has been modelled for some time as applied to brown dwarfs (e.g. Baraffe et al. 2003). 'Cold' start models, where all accretion shock luminosity is radiated away, can have very different initial luminosities, especially for massive planets (e.g. Marley et al. 2007), although detailed shock models considering radiative transfer and reasonable accretion rates have recently shown that 'warm' start models are much more realistic (Marleau, Mordasini & Kuiper 2019). Additionally, models of post-shock gas have shown a zone of stability with initial entropies around 10–11 k_B/baryon, termed 'stalling' accretion (Berardo, Cumming & Marleau 2017). Planets cool and fade as they age but the cooling time is very dependent on the mass and internal entropy of the planet, with high-entropy low-mass planets cooling the fastest, and e.g. a 5 M_J planet cooling at 0.5 k_B/baryon/Myr from an initial internal entropy of 1.5 k_B/baryon (Spiegel & Burrows 2012). Irrespective of these uncertainties in post-formation luminosity evolution, the best time to directly image exoplanets is shortly after their formation, when they are at their highest luminosity. The canonically young age of the TMC provides a perfect environment in which to search for these planets.

In Section 2, we describe our survey sample of 55 stars in the TMC using the Near Infrared Camera (NIRC2) on the Keck II telescope in 2015 and 2016. In Section 3, we describe our observation, data reduction, and small angle analysis methods. In Section 4, we expand our analysis to wider separations and identify companions. Section 5 combines our methods for all separations to place limits on the frequency of wide planets. Our conclusions are presented in Section 6.

2 SURVEY SAMPLE

In choosing our sample of stars in the TMC, we decided to only select single stars, which we define as stars with no known stellar companion within 1 arcsec. The reason for this is first, that multiple-star systems can cause issues with adaptive optics but also for reasons of simplicity. The data reduction and analysis is simplified if there is only one bright central star to consider and there is less theoretical complexity regarding models of planet formation. An exception to this is V410 Tau (Ghez, White & Simon 1997), which we use to ensure we are correctly oriented and to verify our data processing pipelines. Note that we include close ($\lesssim$1 au) spectroscopic binaries in our sample if they meet all other criteria, as we argue wide companions in these systems are likely to be unaffected by the dynamics of the close orbit. Two known systems are in our sample: DQ Tau (Mathieu et al. 1997) and UZ Tau A (Prato et al. 2002).

We primarily consider class II targets because, at this stage in stellar evolution, circumstellar discs have been observed to have very low mass, between 0.2 per cent and 0.6 per cent of the host-star mass (Andrews et al. 2013). This indicates, if there is planet formation, the most massive planets will have already formed by this phase. We also consider class I objects such as HL Tau, which has a circumstellar disc containing notable gaps and rings, which may be indicative of planet formation (Brogan et al. 2015). Our targets were taken from Kraus et al. (2011). We selected targets based on their $J-K$ magnitude colours and only selected targets with $J-K<4$ and K magnitude <10 which can be used as a guide for the approximate L' magnitude. We also made a cut on the spectral type, excluding targets listed as later than M3 in Kraus et al. (2011). This cut-off was chosen to include the relatively abundant low-mass stars in the TMC while cutting out stars that would be too faint for AO observations and too low in mass to expect giant planets. We note that recent studies have produced updated spectral types. The spectral types shown in Table 1 are taken from Herczeg & Hillenbrand (2014) and include one star that is now believed to be later than M3.

All of our targets were observed with an L' filter with the exception of RY Tau, AB Aur, UX Tau, and SU Aur. These stars were observed with a PAH filter as they are too bright for the method described in Section 3.3 to work properly. Our targets are mapped out in Fig. 1 and shown on an H–R diagram in Fig. 2. The map in Fig. 1 also includes the distances taken from *Gaia* and a map of dust reddening from Schlafly et al. (2014). The H–R diagram in Fig. 2 plots the absolute magnitude in the J band (corrected for extinction using models from Fitzpatrick & Massa 2007) against effective temperature. The effective temperature was calculated using spectral types from Herczeg & Hillenbrand (2014). Isochrones and isomass curves are shown using models from Baraffe et al. (2015). Note that several of our targets below 5000 K are underluminous and appear older than 10 Myr. This is due to local reddening that is not taken into account and should not be regarded as the actual age of the star.

As shown in Fig. 1, most of our targets are in the main region of the TMC at distances of 130–150 pc. There are some outliers, most notably DQ Tau and DR Tau at distances of ∼190 pc, and separated from the main group. The stellar properties for all of our targets are presented in Table 1. The temperature was converted to mass using the evolutionary tracks from Baraffe et al. (2015).

3 OBSERVATIONS AND IMAGE ANALYSIS

3.1 Observations

Our observations were made using the NIRC2 camera of the Keck II telescope on 2015 November 27 and 28 and December 5 and 2016 November 7–9. As the focus of these observations was to search for close companions, we used the 512 × 512 subarray mode in order to minimize overheads – noting that the readout time would have often decreased our duty cycle by a factor of ∼2 had we used the full array.[1]

In order to account for irregularities in the telescope point spread function (PSF), at least two position angles were required for each object. Weather permitting, every object was observed in four observing blocks: two in the first half of the night and two in the second half. Where possible we avoided the highest elevations where azimuth slew rates are high and telescope vibrations can affect observations. Based on past experience with Keck, our objects were divided into groups of four and observed in the following sequence: A, B, C, D, A, B, C, D which gave us two observations of four objects. The members of the group are determined by their proximity to each other. This sequence is then repeated in the second half of the night. Each observation consisted of a number of frames (usually six)

[1] https://www2.keck.hawaii.edu/inst/nirc2/ObserversManual.html

Table 1. Properties of target stars in the TMC. The spectral types come from Herczeg & Hillenbrand (2014), the masses are calculated using evolutionary tracks from Baraffe et al. (2015), and the W_1 magnitudes are from the WISE catalogue. The distance comes from the *Gaia* DR2.

Name	RA	Dec.	Distance	Mass ($M_\odot$)	SpT	Rp (mag)	K (mag)	W_1 (mag)
IRAS 04108+2910	04 13 57.38	+29 18 19.3	123.5 ± 1.5	0.40	M3.0	14.0	9.36	7.93
FM Tau	04 14 13.58	+28 12 49.2	131.9 ± 0.8	0.24	M4.5	12.5	8.76	8.00
CW Tau	04 14 17.00	+28 10 57.8	132.4 ± 0.7	1.00	K3.0	11.7	7.13	5.80
FP Tau	04 14 47.31	+26 46 26.4	128.5 ± 0.9	0.36	M2.6	11.6	8.87	8.40
CX Tau	04 14 47.86	+26 48 11.0	127.9 ± 0.6	0.37	M2.5	11.5	8.81	8.52
2MASS J04154278+2909597	04 15 42.79	+29 09 59.8	160.0 ± 1.7	0.51	M0.6	12.8	9.38	9.04
CY Tau	04 17 33.73	+28 20 46.8	128.9 ± 0.7	0.38	M2.3	11.4	8.60	7.79
V409 Tau	04 18 10.79	+25 19 57.4	131.4 ± 0.7	0.54	M0.6	11.2	9.03	8.32
V410 Tau	04 18 31.10	+28 27 16.2	130.4 ± 0.9	1.49	K3.0	9.5	7.63	7.36
BP Tau	04 19 15.83	+29 06 26.9	129.1 ± 1.0	0.45	M0.5	10.6	7.74	7.11
V836 Tau	04 19 26.27	+28 26 14.3	169.6 ± 1.2	0.45	M0.8	11.6	8.60	8.19
IRAS 04187+1927	04 21 43.27	+19 34 13.3	148.7 ± 2.2	0.37	M2.4	13.0	8.02	7.11
DE Tau	04 21 55.63	+27 55 06.2	127.4 ± 1.1	0.37	M2.3	10.8	7.80	7.08
RY Tau	04 21 57.41	+28 26 35.5	149.6 ± 5.4	2.41	G0.0	9.9	5.39	4.24
2MASS J04221675+2654570	04 22 16.76	+26 54 57.1	157.6 ± 3.4	0.52	M1.5	14.8	9.01	7.73
FT Tau	04 23 39.19	+24 56 14.1	127.8 ± 0.8	0.37	M2.8	12.4	8.60	7.65
IP Tau	04 24 57.08	+27 11 56.5	130.6 ± 0.7	0.47	M0.6	11.4	8.35	7.71
DG Tau	04 27 04.69	+26 06 16.0	121.2 ± 2.1	0.64	K7.0	10.9	6.99	6.18
DH Tau	04 29 41.56	+26 32 58.3	135.4 ± 1.3	0.37	M2.3	11.4	8.18	7.40
IQ Tau	04 29 51.56	+26 06 44.9	131.3 ± 1.1	0.43	M1.1	12.0	7.78	7.27
UX Tau	04 30 04.00	+18 13 49.4	139.9 ± 2.0	0.89	K0.0	10.3	8.92	6.92
DK Tau	04 30 44.25	+26 01 24.5	128.5 ± 1.0	0.52	K8.5	11.3	7.10	6.12
IRAS 04278+2253	04 30 50.28	+23 00 08.8	135.4 ± 1.3	1.24	G8.0	11.4	5.86	4.53
JH 56	04 31 14.44	+27 10 17.9	127.5 ± 0.7	0.64	K8.0	11.0	8.79	8.74
LkHa 358	04 31 36.14	+18 13 43.3	102.6 ± 5.1	0.50	M0.9	16.1	9.69	8.21
HL Tau	04 31 38.44	+18 13 57.7	136.7 ± 2.2	0.79	K3c	15.7	7.41	5.24
HK Tau	04 31 50.57	+24 24 18.1	133.3 ± 1.6	0.47	M1.5	12.8	8.59	7.82
2MASS J04321540+2428597	04 32 15.41	+24 28 59.8	130.5 ± 3.2	0.67	K5.5	13.6	8.10	6.62
FY Tau	04 32 30.58	+24 19 57.3	130.2 ± 1.2	0.51	M0.1	12.5	8.05	7.32
FZ Tau	04 32 31.76	+24 20 03.0	130.0 ± 1.3	0.50	M0.5	12.5	7.35	6.15
UZ Tau A	04 32 42.88	+25 52 31.9	131.2 ± 1.6	0.39	M1.9	11.2	7.35	6.25
GI Tau	04 33 34.06	+24 21 17.1	130.5 ± 0.8	0.46	M0.4	11.5	7.89	7.09
DL Tau	04 33 39.08	+25 20 38.1	159.3 ± 1.2	0.99	K5.5	11.1	7.96	6.94
HN Tau A	04 33 39.35	+17 51 52.4	136.6 ± 2.9	0.79	K3c	12.5	8.38	7.23
DM Tau	04 33 48.73	+18 10 10.0	145.1 ± 1.1	0.35	M3.0	12.0	9.52	9.46
CI Tau	04 33 52.01	+22 50 30.1	158.7 ± 1.2	0.97	K5.5	11.1	7.79	6.76
IT Tau	04 33 54.70	+26 13 27.5	162.0 ± 2.0	0.89	K6.0	12.0	7.86	7.40
AA Tau	04 34 55.42	+24 28 53.2	137.2 ± 2.4	0.45	M0.6	13.1	8.05	7.45
DN Tau	04 35 27.38	+24 14 58.9	128.2 ± 0.9	0.46	M0.3	10.5	8.02	7.66
2MASS J04354093+2411087	04 35 40.94	+24 11 08.8	125.2 ± 2.3	0.58	M0.5	14.2	8.41	7.35
HP Tau	04 35 52.78	+22 54 23.2	177.1 ± 3.4	1.26	K4.0	11.8	7.62	6.02
DO Tau	04 38 28.58	+26 10 49.4	139.4 ± 1.0	0.46	M0.3	11.3	7.30	6.34
LkCa 15	04 39 17.79	+22 21 03.4	158.9 ± 1.2	0.97	K5.5	10.7	8.16	7.50
JH 223	04 40 49.51	+25 51 19.2	139.9 ± 1.1	0.38	M2.8	12.9	9.49	8.94
GO Tau	04 43 03.08	+25 20 18.7	144.6 ± 1.0	0.41	M2.3	12.6	9.33	8.97
DQ Tau	04 46 53.06	+17 00 00.1	197.4 ± 2.0	0.43	M0.6	11.4	7.98	7.09
DR Tau	04 47 06.21	+16 58 42.8	195.7 ± 2.5	0.78	K6.0	10.7	6.87	5.83
DS Tau	04 47 48.60	+29 25 11.2	159.1 ± 1.1	0.46	M0.4	11.1	8.04	7.35
GM Aur	04 55 10.98	+30 21 59.5	159.6 ± 2.1	0.84	K6.0	10.8	8.28	8.30
AB Aur	04 55 45.85	+30 33 04.3	162.9 ± 1.5	1.84	A1.0	6.9	4.23	3.25
SU Aur	04 55 59.39	+30 34 01.5	158.4 ± 1.5	2.65	G4.0	8.8	5.99	5.07
MWC 480	04 58 46.26	+29 50 37.0	161.8 ± 2.0	2.03	A3.0	7.5	5.53	4.87
2MASS J05052286+2531312	05 05 22.86	+25 31 31.2	171.9 ± 2.6	0.45	M1.8	14.1	11.16	9.17
RW Aur A	05 07 49.76	+30 24 03.7	151.9 ± 20.8	1.77	K0c	11.4	7.02	6.25
V819 Tau	05 16 22.30	+27 26 24.2	131.7 ± 1.1	0.61	K8.0	11.1	8.42	8.27

with average exposure times of 30 s, which is composed of a small integration time multiplied by an appropriate number of coadds (snapshots that make up the final image), which also varies depending on the brightness of the target. A summary of our observations is shown in Table 2.

3.2 Data reduction

Starting with our raw 512 × 512 pixel images, we first subtracted the master dark frame for the night and divided by the flat frame. For each observing block, the target was observed in two different dither

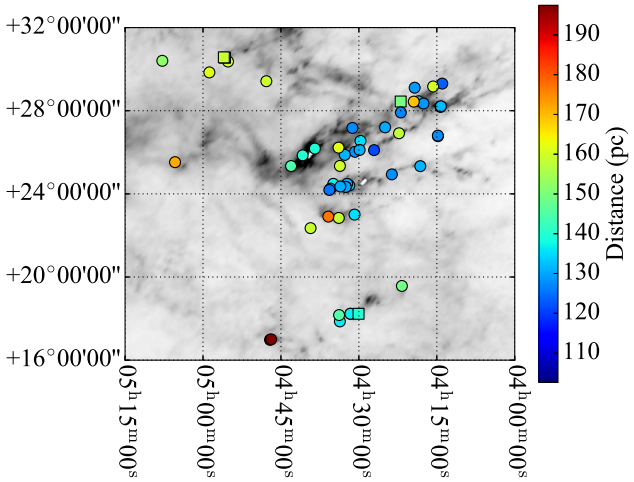

Figure 1. Positions of our targets superimposed on the dust reddening map from Schlafly et al. (2014). The squares represent the bright targets imaged with the PAH filter and circles are all other targets.

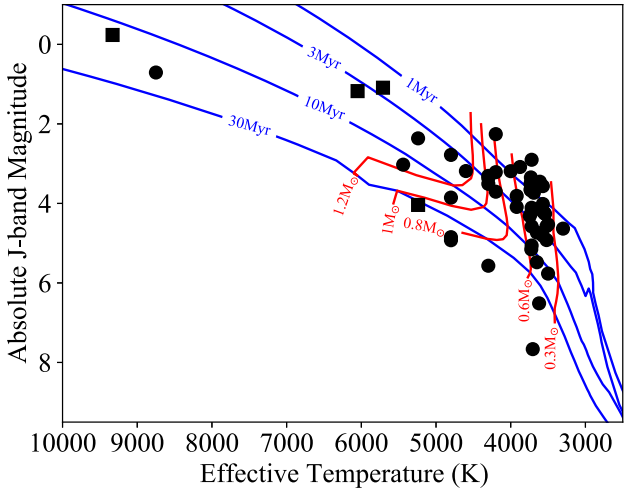

Figure 2. H–R diagram of our targets plotting *R*-band magnitude against effective temperature. As in Fig. 1, the squares represent the bright targets imaged with the PAH filter and circles are all other targets. MWC 480 and AB Aur are A-type stars and are the only stars in our sample hotter than 5000 K, and hence they appear as outliers.

positions. Half the images had the target in the top left quarter and the other half had it in the bottom right corner. This allowed us to calculate an approximate sky background for each image. First, each image was cropped to a size of 192 × 192 pixels (1.92 arcsec × 1.92 arcsec), which was centred on the star by calculating the peak of the image after applying a median filter and performing a simple pixel roll. The corresponding area from the other dither position served as the sky background, which was then subtracted from the cropped image.

Any 'bad' pixels were fixed using the algorithm from Ireland (2013). Once identified, these pixels were set to the corresponding value in the median filtered image. In addition to bad pixels identified in the dark and flat-field images, we also corrected with the same algorithm pixels near saturation that were defined as any with counts greater than 17 500× the number of coadds for that image. The threshold of 17 500 was chosen empirically to produce final PSF-subtracted images with the lowest residuals. Pixels above this threshold were treated as bad pixels. Once all images had been 'cleaned' in this way, they were stored in a data cube containing all images for a particular observing block. The analysis was then performed on these cleaned images.

3.3 Image analysis using PSF subtraction

Our first method of image analysis is a form of reference star differential imaging (RDI) that focuses on simply removing the effect of the central star in order to look for planets. To achieve this, we first went back to the basics of how an image is created. When the telescope's optical system is applied, we assumed the signal from a planet will look the same as a star but reduced by a contrast ratio. In other words, the star was represented by a PSF given by the properties of the optical system and the planet was represented by the same PSF but scaled by a contrast ratio and shifted by the planet's relative position. In 1D, this image function is given by

$$i(x) = p(x) + cp(x - x_0), \tag{1}$$

where p is the PSF representing a single star, c is the contrast ratio between a planet and the star, and x is a spatial variable with the star at $x = 0$ and the planet at $x = x_0$. The first step in our analysis is the subtraction of the PSF.

For our PSF, we simply used the (cleaned) image of another star, which was taken at a similar time to our target. Another possible approach would be principal component analysis (PCA) in which the PSF is taken from a linear combination of stellar images. The number of components in the analysis is optimized, which has shown promising results in reducing background noise and finding planets (Meshkat et al. 2013; Hunziker et al. 2018). An extreme approach would be to create a linear combination using all our images. We have tried this approach as well as an optimization and found that there was no significant improvement in our signal-to-noise ratio, so we do not report on this here. Instead, we have opted for the opposite extreme, in which we only use one image that is selected by optimization. Due to fewer degrees of freedom, this approach also subtracts a smaller fraction of the flux of a real companion than PCA.

Our targets are observed in blocks, typically consisting of six images each. Every target image is matched with the image of another star, which plays the role of our PSF. The PSF image for each target image was chosen from a selection of nearby observing blocks. For a given target image, we have a set of potential PSFs p_n. For each of these, we calculate the sum of the square of the differences given by

$$\Sigma_n = \sum_{ij} \left(t_{ij} - f_n p_{n,ij}\right)^2, \tag{2}$$

where t is the target image, p_n is the image of another star, which we use as the PSF, and i and j are pixel indices. The scaling factor f_n was chosen such that the target and PSF had the same maximum value so when they are subtracted, the central star cancels out. For a given PSF, this is given by

$$f_n = \frac{\max(t)}{\max(p_n)}. \tag{3}$$

This is calculated for all possible PSF images p_n in our sample, simply based on photon count. Whichever produces the smallest value of Σ_n is chosen as our PSF. When this PSF is chosen, we then calculate the difference between the target and the PSF that has been multiplied by the scaling factor f_n. Following on from equation (1), the difference is represented in 1D by

$$\mathrm{d}(x) = i(x) - p(x) = cp(x - x_0). \tag{4}$$

We can then calculate a smooth contrast ratio as a function of position by cross-correlating the difference function with the PSF.

Table 2. Details of observations. T_{int} refers to the integration time for each coadd. This is multiplied by the number of coadds to get the exposure time for each frame. The # of visits column gives the number of observing blocks taken for that object each night. The number of values in this column is the number of observing nights. The # frames column shows the number of frames for each observing block in the order they were taken. For example, IRAS 04108+2910 was observed on only one night and visited four times with six frames in each block. FM Tau was observed on two nights with three visits on the first night, and one on the second. The blocks taken on the first night had 12, 12, and 6 frames, while the block taken on the second night had 6.

Name	Obs. date	T_{int}(s)	Coadds	Exposure time (s)	# Visits	# Frames
IRAS 04108+2910	2016-11-09	0.4	80	32	4	6, 6, 6, 6
FM Tau	2015-11-27, 2015-11-28	0.3	100	30	3, 1	12, 12, 6, 6
CW Tau	2016-11-07	0.2	160	32	4	6, 7, 6, 6
FP Tau	2016-11-07, 2016-11-09	0.1	320	32	4, 1	6, 6, 6, 6, 6
CX Tau	2016-11-07, 2016-11-09	0.4	80	32	5, 1	6, 6, 6, 6, 6, 6
2MASS J04154278+2909597	2016-11-09	0.4	80	32	4	7, 6, 6, 6
CY Tau	2015-11-27, 2015-11-28	0.3	100	30	3, 2	12, 12, 6, 6, 6
V409 Tau	2016-11-09	0.4	80	32	4	7, 6, 6, 6
V410 Tau	2015-11-28, 2016-11-07	0.2	160	32	1, 1	16, 6
BP Tau	2015-11-27, 2015-11-28	0.15	200	30	3, 1	12, 12, 6, 5
V836 Tau	2015-11-27, 2015-11-28	0.3	100	30	4, 1	6, 6, 6, 6, 6
IRAS 04187+1927	2016-11-08	0.4	80	32	4	6, 10, 8, 6
DE Tau	2015-11-27, 2015-11-28, 2015-12-05	0.3	100	30	2, 2, 2	6, 8, 6, 6, 8, 6
RY Tau	2015-11-27, 2015-11-28	1.0	30	30	1, 4	12, 7, 6, 6, 6
2MASS J04221675+2654570	2016-11-08	0.4	80	32	4	9, 6, 6, 6
FT Tau	2016-11-09	0.4	80	32	4	6, 6, 6, 6
IP Tau	2015-11-27, 2015-11-28, 2015-12-05	0.3	100	30	3, 1, 1	12, 12, 6, 10, 6
DG Tau	2015-11-27, 2015-11-28, 2015-12-05	0.15	200	30	2, 1, 3	6, 6, 6, 15, 4, 6
DH Tau	2016-11-08	0.4	80	32	4	6, 11, 6, 6
IQ Tau	2015-11-27, 2015-11-28	0.15	200	30	3, 1	12, 12, 6, 6
UX Tau	2015-11-28	1.0	30	30	5	10, 6, 6, 6, 6
DK Tau	2015-11-27, 2015-11-28, 2015-12-05, 2016-11-08	0.15	200	30	2, 2, 2, 4	6, 8, 6, 6, 6, 8, 6, 6, 6, 6
IRAS 04278+2253	2016-11-08	0.053	600	31	1	7
JH 56	2015-11-27, 2015-11-28	0.3	100	30	3, 1	12, 12, 6, 6
LkHa 358	2016-11-08, 2016-11-09	0.4	80	32	4, 1	6, 4, 6, 6, 6
HL Tau	2016-11-07, 2016-11-09	0.1	320	32	5, 1	6, 6, 6, 6, 14, 6
HK Tau	2015-11-27, 2016-11-09	0.3	100	30	1, 3	9, 8, 6, 6
2MASS J04321540+2428597	2016-11-07, 2016-11-09	0.2	160	32	2, 2	6, 10, 6, 6
FY Tau	2016-11-08, 2016-11-09	0.4	80	32	3, 1	6, 6, 6, 6
FZ Tau	2016-11-07	0.1	320	32	4	5, 6, 4, 6
UZ Tau A	2016-11-09	0.1	320	32	2	6, 6
GI Tau	2015-11-27, 2015-11-28, 2015-12-05	0.15	200	30	3, 1, 2	12, 12, 6, 6, 6, 4
DL Tau	2015-11-27, 2015-11-28, 2015-12-05	0.15	200	30	2, 2, 1	6, 6, 6, 6, 6
HN Tau A	2016-11-08, 2016-11-09	0.4	80	32	3, 1	6, 6, 6, 6
DM Tau	2015-11-27, 2015-11-28	0.3	100	30	2, 3	6, 6, 12, 12, 12
CI Tau	2015-11-27, 2015-11-28	0.15	200	30	3, 1	12, 12, 6, 6
IT Tau	2015-11-28	0.2	160	32	4	6, 6, 6, 6
AA Tau	2015-11-27, 2016-11-09	0.4	80	32	1, 4	12, 9, 6, 5, 4
DN Tau	2015-11-28, 2016-11-09	0.2	160	32	3, 1	6, 6, 6, 6
2MASS J04354093+2411087	2016-11-08, 2016-11-09	0.4	80	32	3, 1	6, 6, 6, 6
HP Tau	2015-11-27, 2015-11-28, 2015-12-05	0.15	200	30	3, 1, 2	12, 12, 6, 6, 6, 10
DO Tau	2016-11-07, 2016-11-08	0.2	160	32	4, 1	6, 6, 10, 6, 6
LkCa 15	2015-11-27, 2015-11-28, 2016-11-08	0.3	100	30	3, 2, 4	12, 12, 6, 6, 6, 6, 6, 6, 6
JH 223	2016-11-07, 2016-11-08, 2016-11-09	0.4	80	32	2, 2, 2	6, 6, 9, 6, 6, 6
GO Tau	2016-11-07, 2016-11-08, 2016-11-09	0.4	80	32	2, 1, 1	6, 6, 6, 6
DQ Tau	2015-11-27, 2015-11-28	0.15	200	30	3, 2	12, 8, 6, 10, 8
DR Tau	2015-11-27, 2016-11-09	0.15	200	30	2, 3	12, 6, 6, 6, 6
DS Tau	2015-11-27, 2015-11-28	0.3	100	30	3, 1	6, 6, 6, 6
GM Aur	2015-11-27, 2015-11-28, 2016-11-08	0.3	100	30	4, 2, 1	6, 6, 6, 6, 12, 12, 6
AB Aur	2015-11-28	0.2	160	32	4	6, 6, 6, 6
SU Aur	2015-11-28	1.0	30	30	5	6, 6, 6, 6, 6
MWC 480	2016-11-07, 2016-11-09	0.053	600	31	4, 3	6, 6, 6, 6, 6, 6, 6
2MASS J05052286+2531312	2016-11-08, 2016-11-09	0.4	80	32	2, 2	8, 6, 6, 6
RW Aur A	2016-11-07, 2016-11-09	1.0	30	30	3, 4	8, 6, 5, 6, 6, 6, 6
V819 Tau	2015-11-27, 2015-11-28	0.3	100	30	3, 1	12, 12, 6, 6

This is then divided by the PSF cross-correlated with itself in order to normalize the contrast ratio. The contrast ratio as a function of position is given by

$$c(x_0) = \frac{(\mathrm{d} \star p)(x_0)}{(p \star p)(x_0)}, \tag{5}$$

where $\star$ denotes the cross-correlation operator given by

$$(\mathrm{d} \star p)(x_0) = \int_{-\infty}^{\infty} \mathrm{d}(x)\, p(x + x_0)\, \mathrm{d}x. \tag{6}$$

When we apply this method to the image of one of our targets, this produces a map of the contrast ratio between any features and the

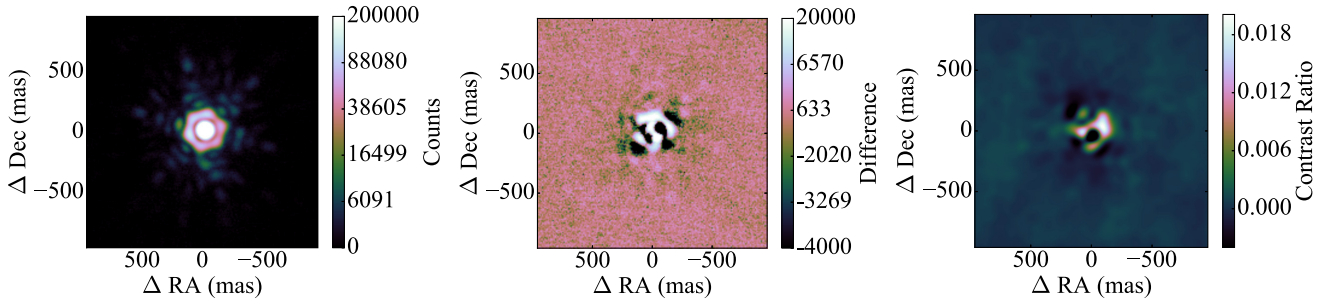

(a) Cleaned Image of AA Tau (b) Difference Image (c) Contrast Map

Figure 3. Example showing a reduced image of AA Tau *(left)*, the difference after an image of HK Tau is subtracted *(centre)*, and the contrast ratio map of AA Tau *(right)*. When the contrast ratio is negative, this is due to positive features in the subtracted image. The bright feature in the middle of the contrast map is due to offsets in the position of the target and PSF central star. At wider separations, we can use this method to search for companions. While there are no obvious features in this example, the contrast values show that we should be able to detect companions more than 0.002 the brightness of the star.

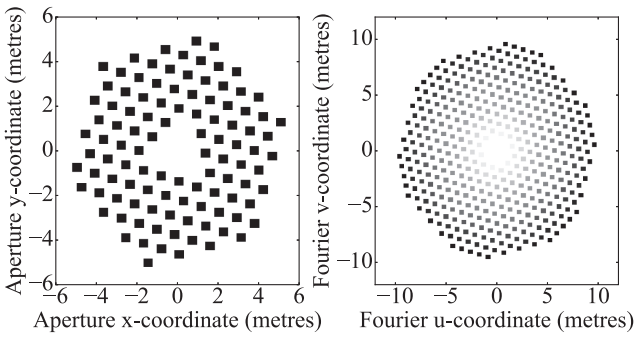

Figure 4. Keck pupil model consisting of 105 individual subapertures (left-hand panel) and its Fourier plane coverage with 205 distinct baselines (right-hand panel) resulting in 100 individual kernel phases. The shading in the right-hand panel shows the redundancy (multiplicity) of the baselines with dark representing low redundancy and bright representing high redundancy. Note that the right-hand panel is the autocorrelation of the left-hand panel (cf. section 2.1 of Martinache 2010).

central star. An example is shown in Fig. 3 with an image of AA Tau. This star was chosen simply because its properties are close to the average of our sample. For the PSF, we used an image of HK Tau which, as shown in Table 2, was taken on the same night.

This process is repeated for all images of the target, and the contrast maps are averaged. By taking the average contrast about an annulus of fixed radius, we then produce a 1D plot of the contrast limit against separation.

3.4 Kernel phase data reduction

Complementary to the PSF subtraction (cf. Section 3.3) we use the kernel phase technique in order to search for companions close to the host star, inside of 500 mas. This analysis begins with the same 192 × 192 pixel cleaned data cubes described in Section 3.3.

The kernel phase technique finds a special linear combination of the Fourier phase ϕ (i.e. the phase of the Fourier transform of the image), which is independent of pupil plane phase φ (phase aberrations in the telescope pupil which cause quasi-static speckles) to second order, similar to closure phase in non-redundant masking, but for full pupil images (i.e. highly redundant apertures). Let $\boldsymbol{A}$ be the baseline-mapping matrix introduced by Martinache (2010), which maps the subapertures in the pupil plane (cf. left-hand panel of Fig. 4) to their corresponding Fourier plane baselines (cf. right-hand panel of Fig. 4), then the Fourier phase ϕ observed through the telescope is

$$\phi = \boldsymbol{R}^{-1} \cdot \boldsymbol{A} \cdot \varphi + \phi_{\rm obj} + \mathcal{O}(\varphi^3), \tag{7}$$

where $\boldsymbol{R}$ encodes the redundancy of the Fourier plane baselines and $\phi_{\rm obj}$ is the phase intrinsic to the observed astronomical object (which is the quantity that we would like to measure). This problem is significantly simplified by multiplying equation (7) with the kernel $\boldsymbol{K}$ of $\boldsymbol{R}^{-1} \cdot \boldsymbol{A}$, i.e.

$$\theta = \boldsymbol{K} \cdot \phi = \underbrace{\boldsymbol{K} \cdot \boldsymbol{R}^{-1} \cdot \boldsymbol{A}}_{=0} \cdot \varphi + \boldsymbol{K} \cdot \phi_{\rm obj} + \mathcal{O}(\varphi^3), \tag{8}$$

so that the kernel phase observed through the telescope θ is directly equal to the kernel phase intrinsic to the observed object $\theta_{\rm obj} = \boldsymbol{K} \cdot \phi_{\rm obj}$ (except for higher order noise terms).

The kernel phase technique was first used by Martinache (2010) who demonstrated the detection of a 10:1 companion at 0.5 λ/D in *HST*/NICMOS data, clearly showing the improved speckle calibration capabilities with respect to image plane data reduction techniques. More recently, Pope et al. (2016) applied kernel phase to ground-based observations of α Oph with the 5.1 m Hale Telescope and showed that it outperforms PSF fitting and bispectral analysis under appropriate conditions (i.e. high Strehl). Kammerer et al. (2019) further developed the technique including a principal component calibration based on Karhunen–Loève decomposition (Soummer, Pueyo & Larkin 2012) for the subtraction of the residual kernel phase signal measured on calibrator stars and detected eight (candidate) low-mass stellar companions (five of which were previously unknown) in an archival VLT/NACO data set, one of which is separated by only 0.8 λ/D.

Here, we use the same kernel phase data reduction pipeline as Kammerer et al. (2019), with slight modifications and improvements explained below.

3.4.1 *Kernel phase extraction*

For extracting the kernel phase from the images, we use the PYTHON library XARA.[2] XARA windows the cleaned images with a super-Gaussian mask, applies a linear discrete Fourier transform to them, and performs a subpixel recentring directly in the complex visibility space afterwards. Then, the Fourier phase ϕ of the images is extracted

[2]https://github.com/fmartinache/xara

and multiplied by the kernel $\boldsymbol{K}$ of the transfer matrix $\boldsymbol{R}^{-1} \cdot \boldsymbol{A}$ of our Keck pupil model (Fig. 4) yielding the kernel phase θ of the images (cf. section 2.1 of Martinache 2010).

For the super-Gaussian mask, we use a radius of 50 pixels (i.e. 500 mas) or a full width at half-maximum of 100 pixels. Our Keck pupil model consists of three individual subapertures per hexagonal Keck primary mirror segment in order to be sensitive to the tip-tilt orientation of each segment. Those subapertures that are behind the central obscuration from the secondary mirror are simply ignored. The subapertures are distributed uniformly in the plane of the primary mirror with a spacing of $b_{\rm min} = 0.9$ m resulting in a field of view of $\lambda/b_{\rm min} \approx 865$ mas and a maximum baseline of $b_{\rm max} = 9.5$ m, yielding a resolution of $\sim\lambda/(2b_{\rm max}) \approx 40$ mas. However, since the super-Gaussian mask has a radius of only 500 mas, we restrict our search for companions (with the kernel phase technique) to angular separations of 40 mas $\leq \rho \leq$ 500 mas.

3.4.2 Kernel phase frame selection

Before we feed the kernel phase extracted from the images into our calibration and model fitting pipeline (cf. Sections 3.4.3 and 3.4.4), we perform a frame selection based on the sum of the squared kernel phase of each image, i.e.

$$\mathrm{SOSK} = \sum_i |\theta_i^2|. \tag{9}$$

From each night, we only keep the 50 per cent best images in the set of potential calibrators and the 75 per cent best images in the set of potential targets, where best means smallest SOSK. This is motivated by the fact that a point-symmetric source (e.g. a single star) has zero Fourier phase ϕ and therefore zero kernel phase θ. Hence, a single star with a faint companion should still have a small kernel phase signal and images with a high kernel phase signal can usually be attributed to bad seeing conditions where the kernel phase technique is not valid (due to too much higher order phase noise). Note that an unknown companion around one of our calibrators would have a small impact only, since we are averaging over a large number of calibrators and do not derotate them before we subtract them from the science target, so that the averaging is destructive in case of pupil-stabilized observations.

3.4.3 Kernel phase calibration

Similar to observations with an interferometer, we have to calibrate the kernel phase of our targets by subtracting the kernel phase of calibrators. This is done using the Karhunen–Loève projection described in section 2.3 of Kammerer et al. (2019). We perform the Karhunen–Loève calibration separately for each night since we found this to yield a smaller reduced χ^2 than calibrating data from multiple nights together. The reason for this is likely that the quasi-static phase aberrations (for which we try to compensate with our calibration) are only stable over time-scales of minutes to hours.

From the 75 per cent best images of each night, we select one object as a target and all images of different objects from the 50 per cent best images of the same night as calibrators. Then, we subtract the first four Karhunen–Loève components from the kernel phase of the target θ and its uncertainties $\boldsymbol{\Sigma}_\theta$, i.e.

$$\theta' = \boldsymbol{P}' \cdot \theta, \tag{10}$$

$$\boldsymbol{\Sigma}'_\theta = \boldsymbol{P}' \cdot \boldsymbol{\Sigma}_\theta \cdot \boldsymbol{P}'^T, \tag{11}$$

where $\boldsymbol{\Sigma}_\theta$ and $\boldsymbol{P}'$ are obtained as described in sections 2.2.3 and 2.3 of Kammerer et al. (2019).

3.4.4 Kernel phase model fitting

After calibrating the kernel phase, we fit the binary model

$$\theta'_{\rm bin} = \boldsymbol{P}' \cdot \boldsymbol{K} \cdot \arg\left(1 + c\exp\left(-2\pi i\left(\frac{\Delta_{\rm RA} u}{\lambda} + \frac{\Delta_{\rm Dec} v}{\lambda}\right)\right)\right), \tag{12}$$

where $0 \leq c \leq 1$ is the companion contrast, $\Delta_{\rm RA}$ and $\Delta_{\rm Dec}$ are the on-sky separation of the companion, u and v are the Fourier coordinates of the pupil model, and $\lambda = 3.776$ µm is the observing wavelength, using a grid search and a least-squares routine as described in section 2.4 of Kammerer et al. (2019). We fit to all images of the same target simultaneously, also when a target was observed during multiple nights. Using the uncertainties $\boldsymbol{\Sigma}'_\theta$ derived from the photon noise of the images this yields an RA–Dec map of best-fitting companion contrasts $\boldsymbol{c}_{\rm fit}$ and their uncertainties $\boldsymbol{\sigma}_{c_{\rm fit}}$ whose ratio is the photon noise-based signal-to-noise ratio $SNR_{\rm ph}$. The grid position with the smallest reduced χ^2 (obtained from a least-squares routine) is our best-fitting companion.

3.4.5 Empirical kernel phase detection limits

If the uncertainties $\boldsymbol{\Sigma}_\theta$ derived from the photon noise would describe the underlying errors correctly (i.e. if all other errors would be negligible), we could simply classify those best-fitting companions whose $SNR_{\rm ph} > 5$ as significant detections. However, although readout noise and dark current are negligible for our data set, there is a lot of higher order phase noise, which leads to a high $SNR_{\rm ph}$ and false detections for all of our targets (cf. column '$SNR_{\rm ph}$' of Table 3). Note that the kernel phase is independent of pupil plane phase noise only to second order and higher order phase noise might be introduced by atmospheric turbulence or imperfect telescope optics.

Hence, an empirical method is necessary to derive robust detection limits. We classify the 1/3 of the targets with the highest $SNR_{\rm scaled}$ as candidate detections and the rest of the targets as calibrators (cf. columns 'Can?' and 'Cal?' of Table 3). Here, $SNR_{\rm scaled}$ is the photon noise-based SNR scaled by the K-band magnitude of the object, i.e.

$$\mathrm{SNR}_{\rm scaled} = \mathrm{SNR}_{\rm ph}\sqrt{\frac{1}{10^{-(K-K_{\rm med})/2.5}}}, \tag{13}$$

where $K_{\rm med}$ is the median K-band magnitude of our targets. This scaling is motivated by the fact that the brighter objects have higher photon noise-based SNRs due to smaller uncertainties, but similar quasi-static errors. Then, we repeat the Karhunen–Loève calibration (only allowing images of objects in the list of calibrators to be selected as calibrators) and the model fitting. Afterwards, we compute an empirical detection limit $\boldsymbol{\sigma}_{\rm emp}$ and an empirical signal-to-noise ratio,

$$\mathrm{SNR}_{\rm emp} = \frac{\boldsymbol{c}_{\rm fit}}{\boldsymbol{\sigma}_{\rm emp}} \tag{14}$$

for each of the candidate detections as described in section 2.4.3 of Kammerer et al. (2019) and classify a candidate detection as significant, if $SNR_{\rm emp} > 5$. Note that this empirical detection limit is based on azimuthally averaging the contrast maps $\boldsymbol{c}_{\rm fit}$ and therefore is primarily sensitive to point-like emission. Detecting extended structure (such as discs) would require a more sophisticated approach, yielding higher sensitivities.

Table 3. Results of our kernel phase analysis when classifying the 1/3 most significant detections based on SNR_{scaled} as candidate detections ('Can?') and the rest as calibrators ('Cal?') for the empirical detection method. Candidate detections with an empirical detection significance $SNR_{emp} > 5$ are classified as significant detections ('Det?').

Name	SNR_{ph}	SNR_{scaled}	Can?	Cal?	SNR_{emp}	Det?
IRAS 04108+2910	25.6	46.9	N	Y	–	N
FM Tau	23.5	32.8	N	Y	–	N
CW Tau	112.8	74.1	N	Y	–	N
FP Tau	23.9	35.0	N	Y	–	N
CX Tau	25.5	36.3	N	Y	–	N
2MASS J04154278+2909597	13.4	24.9	N	Y	–	N
CY Tau	25.2	32.5	N	Y	–	N
V409 Tau	21.3	33.6	N	Y	–	N
V410 Tau	450.3	372.4	Y	N	122.7	Y
BP Tau	36.5	31.7	N	Y	–	N
V836 Tau	23.6	30.4	N	Y	–	N
IRAS 04187+1927	131.8	130.5	Y	N	4.2	N
DE Tau	144.4	129.2	Y	N	2.0	N
2MASS J04221675+2654570	25.0	39.1	N	Y	–	N
FT Tau	33.3	43.0	N	Y	–	N
IP Tau	26.4	30.4	N	Y	–	N
DG Tau	1097.7	677.0	Y	N	3.5	N
DH Tau	28.3	30.2	N	Y	–	N
IQ Tau	42.2	37.4	N	Y	–	N
DK Tau	434.7	281.3	Y	N	1.8	N
JH 56	10.5	14.8	N	Y	–	N
LkHa 358	52.9	112.8	Y	N	2.1	N
HL Tau	433.7	324.3	Y	N	4.9	N
HK Tau	38.1	49.1	N	Y	–	N
2MASS J04321540+2428597	85.9	88.2	N	Y	–	N
FY Tau	66.8	67.2	N	Y	–	N
FZ Tau	194.3	141.1	Y	N	2.6	N
UZ Tau A	318.8	231.9	Y	N	1.4	
GI Tau	43.2	40.2	N	Y	–	N
DL Tau	66.9	64.5	N	Y	–	N
HN Tau A	80.4	94.2	N	Y	–	N
DM Tau	11.6	23.0	N	Y	–	N
CI Tau	89.6	79.9	N	Y	–	N
IT Tau	37.6	34.6	N	Y	–	N
AA Tau	175.2	175.6	Y	N	2.3	N
DN Tau	46.5	45.9	N	Y	–	N
2MASS J04354093+2411087	80.1	94.9	Y	N	1.6	N
HP Tau	79.0	65.2	N	Y	–	N
DO Tau	181.2	129.0	Y	N	3.2	N
LkCa 15	117.2	124.0	Y	N	3.1	N
JH 223	15.2	29.7	N	Y	–	N
GO Tau	19.4	35.2	N	Y	–	N
DQ Tau AB	58.9	57.3	N	Y	–	N
DR Tau	272.8	159.3	Y	N	1.4	N
DS Tau	40.2	40.1	N	Y	–	N
GM Aur	39.6	44.2	N	Y	–	N
MWC 480	1244.7	391.0	Y	N	1.6	N
2MASS J05052286+2531312	13.0	54.8	N	Y	–	N
RW Aur A	571.5	357.0	Y	N	3.6	
V819 Tau	17.1	20.4	N	Y	–	N

3.5 Comparison of both methods

The 1D contrast plot (given for each separation by averaging around an annulus of fixed radius) is shown for both the PSF subtraction and kernel phase methods at the 5σ level for two stars: AA Tau and CX Tau in Fig. 5. As theoretically expected, Fig. 5 demonstrates that the kernel phase method outperforms the PSF subtraction method over its effective range of ∼0.5 arcsec and the latter method is only useful at wider separations. This was the case for all of our targets. Our contrast limits for both methods indicate that we cannot detect objects fainter than ∼1/2000 the brightness of the star even at separations of 0.5 arcsec, which is insufficient for the detection of core-accreting giant planets (Wallace & Ireland 2019).

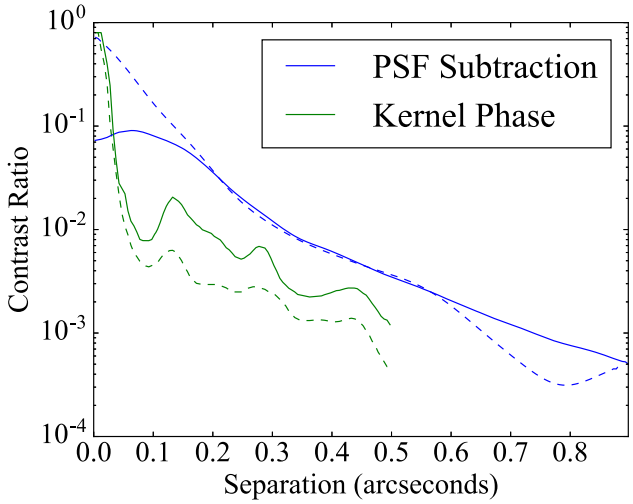

Figure 5. The 5σ contrast limit for AA Tau (*solid curve*) and CX Tau (*dashed curve)* as a function of separation from the star. This shows, for example, at a separation of 0.3 arcsec from AA Tau, the PSF subtraction method cannot detect anything less than 1/100 the brightness of the star but kernel phase can achieve limits of 1/300 the brightness of the star.

3.6 Significant features from kernel phase analysis

The kernel phase analysis revealed several features, of which we define those with an empirical $SNR_{\rm emp} > 5$ as significant detections. This criterion was only met by V410 Tau, which has a known brown dwarf companion (Ghez et al. 1997). We detect this known companion with both of our methods (cf. Fig. 6). The kernel phase technique yields very precise constraints on its position and contrast, obtained from a Markov chain Monte Carlo (MCMC) fit (cf. Fig. 7), and its best-fitting parameters are listed in Table 4.

Note that, as shown in Table 3, HL Tau has a feature with $SNR_{\rm emp} = 4.9$ so only just falls short of our detection threshold. We believe this to be a feature of HL Tau's large protoplanetary disc (ALMA Partnership 2015) and not a companion.

4 WIDE SEPARATION ANALYSIS

Due to a focus on efficient observations at small angles (see Section 3.1), these data were mostly taken in a subarray readout mode, limiting the field of view. We further extended our analysis to wider angles that were not covered by the 192 × 192 pixel cleaned images and analysis shown in Section 3.3. At these separations beyond ∼0.8 arcsec, PSF features were almost non-existent so we could use a more conventional image analysis with a simplified PSF model.

To clean these full images, our image reduction simply consisted of dividing by a master flat and correcting bad pixels. The master flat was created from all dithered observations for a night, using pixels significantly away from detected objects. Companions were searched for over an (ρ, θ) grid in polar sky coordinates by performing aperture photometry with a simplified Gaussian PSF model, as described below. This truncated PSF model enabled searching for companions closer to the image edge.

For each tested grid point, including the central star (i.e. separation ρ of 0), we found a least-squares solution to the flux F of a model:

$$d_k = B + F g_k, \tag{15}$$

where d_k is the data for pixel k over a 16 × 16 pixel grid, g_k is a normalized Gaussian function with width matched to the observed PSF, and B the background. This least-squares flux solution for F is simply given by

$$F = \frac{\Sigma_k (g_k - \Sigma g_k/N) d_k}{\Sigma_k (g_k - \Sigma g_k/N) g_k}, \tag{16}$$

where $N = 256$, the total number of pixels. The uncertainty in pixels k was simply estimated by the root mean square residuals of the fit, and the uncertainty in F obtained by standard error propagation assuming independent background-limited uncertainties for all pixels. These fluxes were converted to contrasts by dividing by the fitted flux at a separation of 0, and these (ρ, θ) contrast maps averaged together with inverse variance weighting. Finally, uncertainties were corrected at each radius ρ to ensure that the median absolute deviation of the residuals at every radius matched that of a unit Gaussian.

By highlighting features with significance greater than 7σ and removing those that can be explained by the few residual speckles, we are able to determine the approximate positions of companions to our targets. The contrast and position of each companion is calculated by fitting to the original reduced images. We are able to detect significant companions for nine of our objects, the properties of which are listed in Table 5.

The companion of DH Tau is the only substellar-mass companion we are able to detect and our contrast is consistent with other studies such as Kraus et al. (2013). We also find a high-contrast companion to HK Tau. The fitted contrast maps for DH Tau and HK Tau are shown in Fig. 8.

Despite the high contrast of the companion to HK Tau, previous studies have concluded that it is a stellar mass companion of similar spectral type to the primary and is obscured by an edge-on circumstellar disc (Stapelfeldt et al. 1998). This circumstellar disc is represented by the elongated shape of the companion. Although we did not detect any additional brown dwarf mass companions to our targets, we now have a more complete picture of our contrast limits at wide separations. These contrast limits are listed in Table 6. Fig. 9 shows the contrast curves for all targets with the detected companions indicated. The companion to HK Tau is marked with a red circle and other companions are marked with blue squares.

Assuming an age of 1 Myr for our planets, which is conservative as they may still be forming in a Class II disc, we converted the contrast into a mass limit using models from Spiegel & Burrows (2012). For this conversion, we need to assume an appropriate internal entropy for our planets. As mentioned previously, planet luminosity and internal entropy is highly uncertain but recent models suggest few Jupiter mass planets have initial entropy no less than ∼10–11 $k_{\rm B}$/baryon (e.g. Mordasini 2013; Berardo et al. 2017; Marleau et al. 2019). The hot-start and cold-start entropy curves take the form of a 'tuning fork' with hot-start entropy increasing with mass and cold-start entropy decreasing with mass (Marley et al. 2007). However, since hot-start models are expected to be more likely for high-mass planets due to the difficulty in radiating away the accretion luminosity for all but the lowest accretion rates, a reasonable assumption is that the average entropy is fairly constant at somewhere around 10–11 $k_{\rm B}$/baryon across the 1–10 $M_{\rm J}$ range. To keep our model simple, we assume a single value of initial internal entropy, regardless of mass. Analysis of directly imaged planets indicates β-Pic b, at the high-mass end of the planet distribution, formed with a minimum entropy of ∼10.5 $k_{\rm B}$/baryon (Marleau & Cumming 2014). We have decided to use this value to calculate mass limits as it is also close to the average initial entropy of a 1 $M_{\rm J}$ planet according to Spiegel & Burrows (2012) and can be applied to a wide

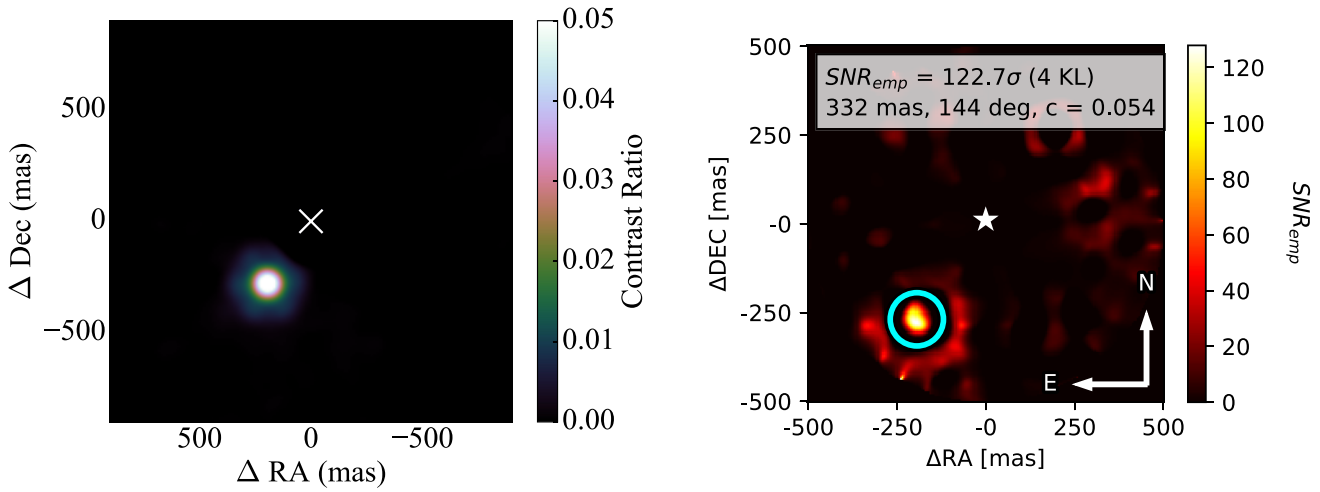

Figure 6. Contrast map of V410 Tau using PSF subtraction (left-hand panel) and kernel phase detection map (right-hand panel). The host star is in the middle of the images and is removed by both methods. The companion is clearly visible to the south-east and consistently detected with both methods. In the kernel phase detection map, V410 Tau B's position is highlighted with a cyan circle and there is a residual halo around it which is caused by the limited Fourier coverage and model redundancies and disappears after subtracting the kernel phase signal of V410 Tau B from the data.

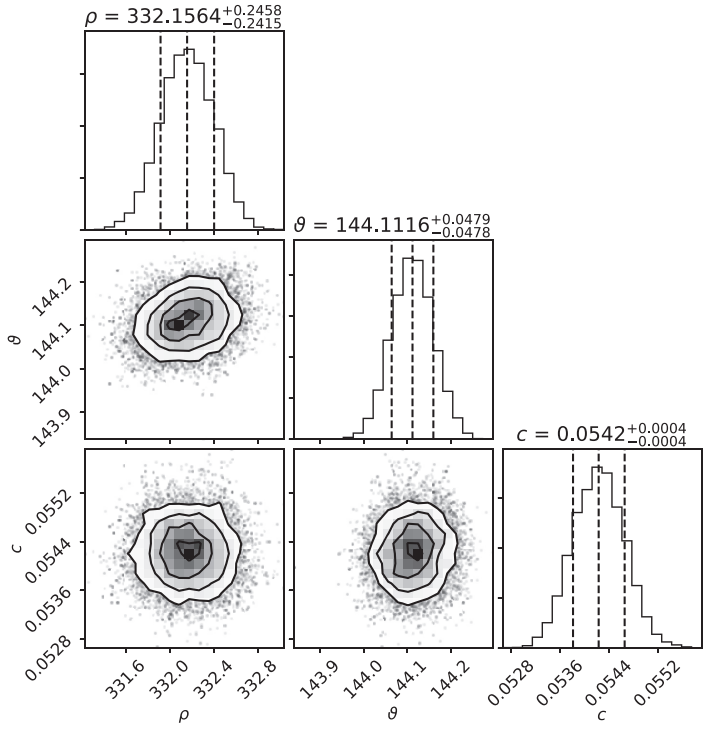

Figure 7. Corner plot (Foreman-Mackey 2016) for an MCMC initialized around the best-fitting position. The three fitted parameters are the angular separation ρ, the position angle θ, and the contrast c. The MCMC is computed from the kernel phase using EMCEE (Foreman-Mackey et al. 2013) with six random walkers initialized around the best-fitting position and a temperature of $f_{\rm err}^2 = (\sigma_{\rm emp}/\sigma_{\rm ph})^2 = 13.4 \approx \chi^2_{\rm red}$, in order to find the best-fitting parameters including their correlated uncertainties by maximizing the log-likelihood of the binary model (cf. Kammerer et al. 2019).

Table 4. Properties of the companion to V410 Tau with uncertainties from the kernel phase analysis.

Name	Sep. (mas)	Pos. ang. (°)	Contrast
V410 Tau B	332.2 ± 0.2	144.11 ± 0.05	0.0542 ± 0.0004

temperature range of 500–1500 K (Berardo et al. 2017). Using this entropy, we calculate planet magnitude as a function of mass and age using Spiegel & Burrows (2012), and thus convert contrast ratio to mass.

Using the stellar masses shown in Table 1, this mass limit was also converted to a mass ratio. This is shown for all targets in Fig. 10.

Table 5. Properties of fitted companions.

Name	Separation (arcmin)	Position Angle (°)	Contrast (Δm)	# Observations
2MASS J04354093+2411087	2.11	175.0	1.98 ± 0.01	1
2MASS J05052286+2531312	2.35	59.8	2.24 ± 0.01	2
DH Tau	2.35	139.0	5.75 ± 0.02	1
DK Tau	2.39	119.5	1.81 ± 0.01	4
HK Tau	2.25	169.9	5.27 ± 0.02	1
IRAS 04278+2253	1.29	95.9 ± 0.6	2.00 ± 0.02	1
IT Tau	2.43	225.8	1.64 ± 0.01	1
JH 223	2.15	342.2	2.40 ± 0.01	3
RW Aur A	1.49	254.6 ± 0.1	2.42 ± 0.01	2

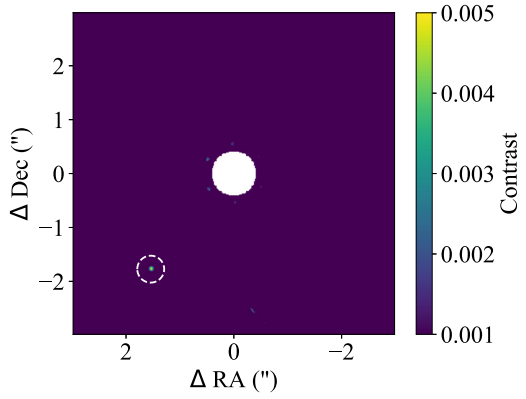

(a) Fitted Contrast Map of DH Tau

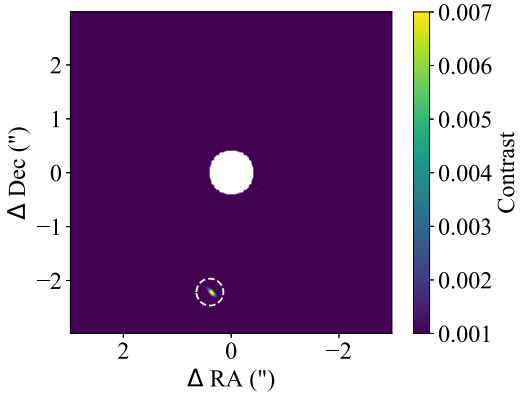

(b) Fitted Contrast Map of HK Tau

Figure 8. Contrast maps of DH Tau and HK Tau with the companions circled.

As shown in Figs 9 and 10, the companion to DH Tau is close to the faintest we were able to detect. Note while the companion to HK Tau is included (shown with a red circle), the circumstellar disc reduces its brightness so the true mass is probably much higher than that shown in Fig. 10. The top panel of Fig. 10 shows that we are able to detect planetary-mass companions ($<13\,M_J$) for most of our targets at wide separations (>100 au). The lack of new brown dwarf detections from our data implies these companions are rare at wide separations, providing evidence of the 'brown dwarf desert' described by Marcy & Butler (2000) and Grether & Lineweaver (2006). The lack of planetary-mass detections allows us to constrain the maximum frequency of hot-start planets in the TMC.

5 THE FREQUENCY OF WIDE SEPARATION MASSIVE PLANETS

5.1 Total probability of planet detection

Despite our lack of planet detections, Fig. 10 shows that our limits are sufficient for the detection of young planetary-mass companions for many of our targets. This opens up the possibility of detecting wide systems analogous to HR 8799. Combining the contrast limits for all of our targets, we can determine the likelihood of detecting a planet as a function of mass and semimajor axis. We apply the same method as Fig. 10 with an age of 1 Myr and initial entropy of $10.5\,k_B$/baryon to convert magnitude to mass using models from Spiegel & Burrows (2012). Using Monte Carlo sampling, we randomize the system inclination and planet positions to get a more comprehensive view of our capabilities. This is shown in Fig. 11. The HR 8799 planets are shown, as well as the $13\,M_J$ planet-mass threshold.

5.2 Comparison with HR 8799 analogues

The result in Fig. 11 shows that, averaged over all targets, we have a greater than 80 per cent probability of detecting $>10\,M_J$ planets at separations beyond 100 au. However, even at the lower mass and separations of an HR 8799 analogue, we still have a ∼20 per cent chance of detecting this system at an age of 1 Myr with an initial internal entropy of $10.5\,k_B$/baryon. Applying the luminosity curves from Spiegel & Burrows (2012) to our HR 8799 analogue, we determine the probability of detecting these planets at ages of 0–3 Myr. Our detection probability of the four planets around HR 8799 is shown in Fig. 12.

The curves in Fig. 12 demonstrate how the planets around HR 8799 cool and fade over time. When the planets are newly formed, we have a greater than 40 per cent chance of detecting HR 8799 b and c analogues. At an age of 3 Myr, we only have a 30 per cent chance of detecting these planets.

The stars in our sample are believed to have an age of ∼2–3 Myr, which implies any planets around our targets are not much older than ∼1 Myr. Since no planets were detected in our sample, we can make a statement on the maximum frequency of wide and massive systems.

5.3 Planet frequency

We use the same method from Vigan et al. (2012) to calculate the maximum planet frequency in a given range. This method assumes the likelihood of the data d for a given frequency f is given by

$$L(\{d_i\}\,|\,f) = \prod_i^N (1 - fp_i)^{1-d_i} (fp_i)^{d_i}, \quad (17)$$

Table 6. Contrast limits for our targets using all three methods.

	Contrast Limit (Δm)						
Name	0.1 arcsec	0.3 arcsec	0.5 arcsec	0.7 arcsec	1 arcsec	1.5 arcsec	2 arcsec
IRAS 04108+2910	5.09	6.03	6.79	6.52	7.40	7.66	7.13
FM Tau	5.49	6.64	7.10	6.85	7.87	7.85	7.67
CW Tau	4.94	7.14	8.41	6.58	9.24	9.82	9.87
FP Tau	5.54	7.06	8.04	7.26	7.93	7.65	7.57
CX Tau	5.84	6.55	8.31	8.06	8.15	7.85	7.64
2MASS J04154278+2909597	5.68	6.02	7.01	6.40	6.35	6.79	6.35
CY Tau	5.29	7.25	8.14	7.57	8.45	7.92	7.25
V409 Tau	5.60	6.78	7.63	7.13	7.68	7.96	7.45
V410 Tau	4.88	3.54	5.60	7.03	5.75	6.53	4.96
BP Tau	5.54	7.51	8.49	7.89	9.43	9.00	8.82
V836 Tau	5.00	6.59	7.43	7.12	8.05	7.98	7.86
IRAS 04187+1927	4.68	6.42	7.84	7.82	8.31	8.82	9.06
DE Tau	4.67	6.70	7.96	7.59	9.02	9.13	8.98
RY Tau	6.01	8.07	9.69	10.10	8.27	9.19	9.47
2MASS J04221675+2654570	5.59	6.39	7.61	7.50	8.39	8.76	8.20
FT Tau	5.61	6.36	7.41	7.20	8.28	8.64	8.17
IP Tau	6.29	7.09	8.16	6.90	7.51	7.27	7.37
DG Tau	3.91	6.26	7.11	6.84	8.30	7.39	9.80
DH Tau	6.05	6.15	7.93	7.62	8.57	8.06	8.47
IQ Tau	6.57	6.49	8.08	7.83	8.89	8.94	8.77
UX Tau	6.34	8.25	8.73	8.99	6.55	6.39	5.97
DK Tau	5.05	6.24	7.71	7.72	8.69	9.11	9.13
IRAS 04278+2253	3.29	4.33	5.13	5.45	6.62	7.43	8.73
JH 56	6.56	7.15	7.64	6.80	7.81	7.73	7.42
LkHa 358	3.92	5.59	6.61	6.94	8.39	7.39	7.58
HL Tau	4.90	6.16	7.37	7.26	8.47	10.36	10.43
HK Tau	5.21	6.57	7.66	7.47	7.29	7.36	7.13
2MASS J04321540+2428597	5.10	6.59	7.56	7.53	8.75	9.60	9.38
FY Tau	5.44	6.77	7.71	8.14	8.92	8.81	8.87
FZ Tau	5.18	6.37	7.23	7.59	9.31	10.15	9.71
UZ Tau A	3.99	5.89	7.01	7.08	9.21	9.62	9.01
GI Tau	5.48	7.23	8.30	7.39	7.41	7.50	8.51
DL Tau	5.20	7.12	8.18	8.04	9.29	9.51	9.21
HN Tau A	5.07	6.47	7.37	7.79	8.70	9.07	8.92
DM Tau	5.51	6.27	6.95	6.85	7.23	7.17	6.83
CI Tau	5.71	7.24	8.05	8.40	9.02	9.36	9.17
IT Tau	4.39	6.15	7.55	7.61	8.64	8.70	8.50
AA Tau	4.99	6.01	7.25	7.33	8.51	8.42	8.16
DN Tau	6.90	7.22	8.05	7.27	9.19	8.99	8.64
2MASS J04354093+2411087	5.21	6.13	6.87	7.63	8.91	9.07	7.51
HP Tau	5.17	6.28	7.89	7.20	6.66	6.11	5.38
DO Tau	4.86	6.05	7.88	7.34	8.62	9.36	9.70
LkCa 15	4.82	6.00	7.54	8.34	7.38	7.36	7.82
JH 223	6.11	6.92	7.36	7.16	7.44	7.10	6.71
GO Tau	5.48	6.81	7.29	6.81	7.53	7.35	7.16
DQ Tau	5.55	7.30	8.04	8.57	9.07	9.18	8.63
DR Tau	4.82	6.32	7.57	7.96	9.14	10.30	10.09
DS Tau	6.12	6.71	7.78	7.52	8.76	8.91	8.84
GM Aur	5.27	6.99	8.25	7.62	8.37	8.07	8.09
AB Aur	6.40	8.58	9.40	9.86	7.75	9.83	9.26
SU Aur	5.72	7.95	9.25	9.75	8.73	8.16	8.09
MWC 480	4.76	6.13	6.81	7.34	8.86	10.34	10.52
2MASS J05052286+2531312	5.00	6.04	6.53	6.59	6.63	6.49	6.84
RW Aur A	4.55	5.92	7.02	7.10	9.06	5.23	10.32
V819 Tau	6.07	7.08	7.92	7.63	8.42	8.36	7.97

where N is the number of targets, in our case 55, d_i is 0 if no planets are detected and 1 if at least 1 planet is detected. The probability p_i is the probability of detecting planets in a given range assuming an appropriate planet distribution. We assume a power-law distribution in mass and semimajor axis such that

$$\frac{\mathrm{d}N_{\mathrm{planets}}}{\mathrm{d}\ln M \mathrm{d}\ln a} = C M^{\alpha} a^{\beta}. \quad (18)$$

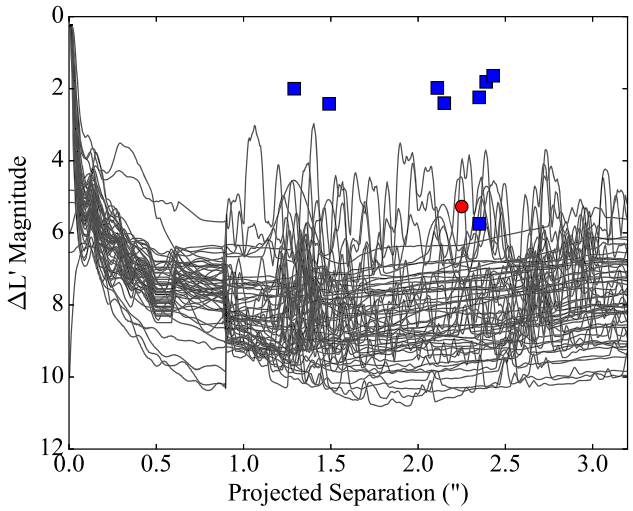

Figure 9. 5σ contrast curves for all targets including contrast and separation of detected companions. Each line is our contrast limit for a particular target and the markers show detected companions. The red circle indicates the companion to HK Tau.

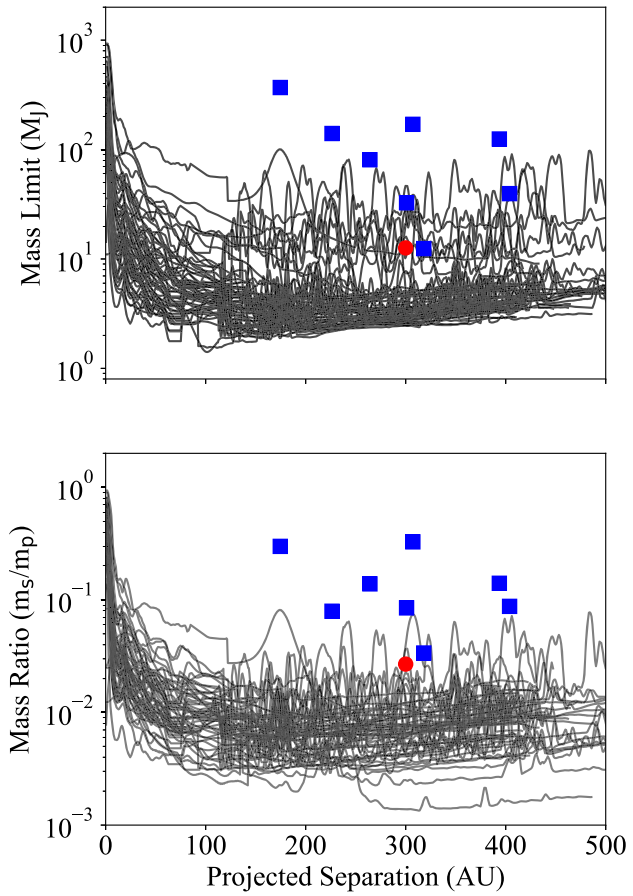

Figure 10. Mass and mass ratio limits for all targets. The companion to HK Tau is again represented by a red circle as the actual mass is assumed to be higher than shown here.

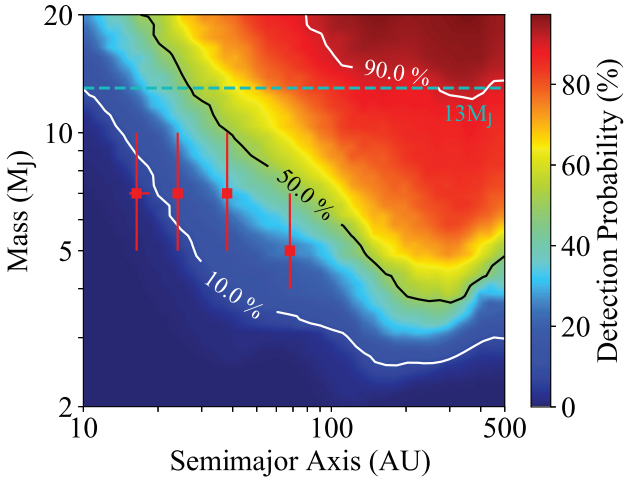

Figure 11. Probability of planet detection as a function of mass and semimajor axis for a planet age of 1 Myr and initial internal entropy of 10.5 k_B/baryon. The HR 8799 planets and the planet-mass threshold of 13 M_J are also shown.

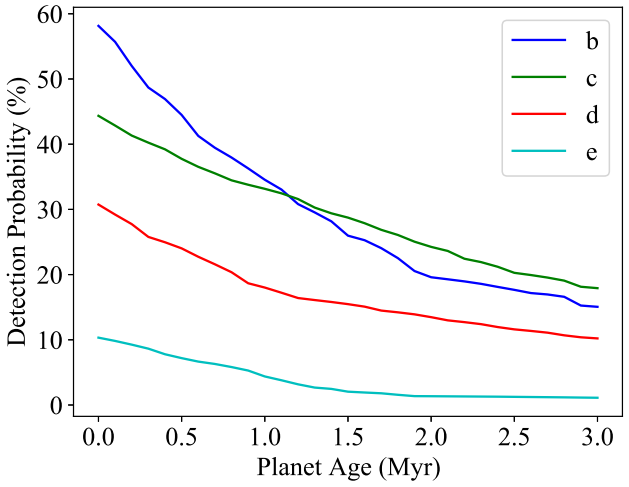

Figure 12. Detection probability of HR 8799 analogues (averaged over all targets) versus age of the planets. An age of 0 corresponds to the moment the planets stop accreting.

We obtain the posterior distribution from Bayes' theorem:

$$p(f|\{d_i\}) = \frac{L(\{d_i\}|f)p(f)}{\int_0^1 L(\{d_i\}|f)p(f)df}, \quad (19)$$

where $p(f)$ is the priori probability density of the frequency f which we set to a uniform value of 1. For a given confidence level, the maximum frequency is obtained using

$$\text{Confidence} = \int_{f_{\min}}^{f_{\max}} p(f|\{d_i\})df. \quad (20)$$

We set $f_{\min}$ to 0 and rearrange to find $f_{\max}$. This value was calculated over a semimajor axis range of 10–500 au, the same as Fig. 11, and a mass range of 2–13 M_J. Since we did not detect any planets in this range, all of our values of d_i will be 0. To obtain our probabilities p_i, we try several values for the mass and semimajor axis power-law indices while keeping the range constant at [2,13] M_J and [10,500] au. The planet age is again set to be 1 Myr and the initial internal

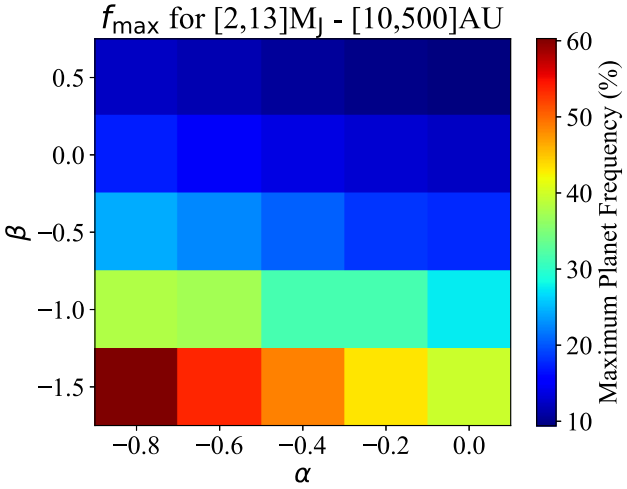

Figure 13. Maximum planet frequency for mass 2–13 M_J and semimajor axis 10–500 au at 90 per cent confidence with differing mass and semimajor axis power-law indices (α and β, respectively).

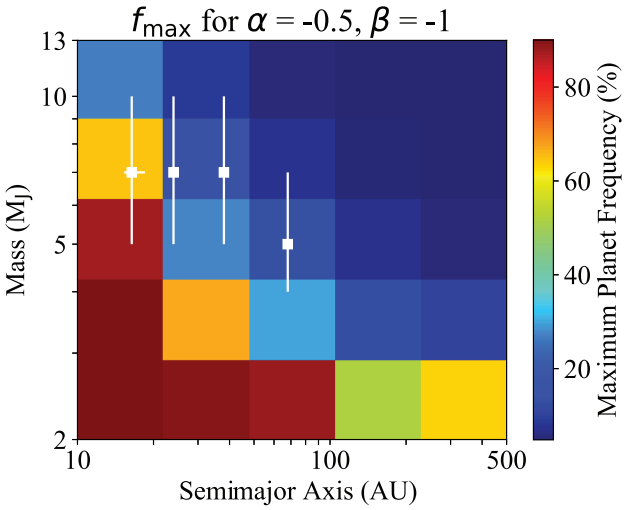

Figure 14. Maximum planet frequency assuming a power law with $\alpha = -0.5$ and $\beta = -1$ at 90 per cent confidence. The white points show the planets around HR 8799.

entropy is 10.5 k_B/baryon. The maximum frequency at a 90 per cent confidence level is shown in Fig. 13.

As shown in Fig. 13, the maximum frequency is better constrained at higher power-law indices but these are considered unlikely power-law indices at this mass and semimajor axis range. The symmetric power law given by Fernandes et al. (2019) has a mass index of $\alpha = -0.45$ and a semimajor axis index of $\beta = -0.95$. The study from Bowler & Nielsen (2018) has $\alpha = -0.65$ and $\beta = -0.85$. Our result shows that less than ∼30 per cent of stars have a planet in this mass and semimajor axis range if we assume one of these power-law distributions.

Assuming a power-law distribution in which $\alpha = -0.5$ and $\beta = -1$, we also calculate the dependence of planet frequency on mass and semimajor axis. This is shown in Fig. 14 over a mass range of 2–13 M_J and semimajor axis range of 10–500 au at a 90 per cent confidence level. The planets around HR 8799 are also marked.

The result from Fig. 14 confirms that massive planets at wide separations are very rare, occurring around less than 10 per cent of stars. Planets with the mass and semimajor axis similar to HR 8799 b, c, and d are expected to occur around less than 20 per cent of stars, while analogues to HR 8799 e may be more common, but we cannot draw a strong conclusion from our results regarding this aspect.

6 SUMMARY AND CONCLUSIONS

In this work, we have conducted a high-contrast imaging survey of the TMC with the aim of finding any massive young planets and planets in the process of forming. Using the PSF subtraction technique, we found that our limits are not sufficient to detect planetary-mass companions at small separations. The kernel phase method improved our limits at small separations, but was still insufficient for detection of Solar system analogues. For non-accreting planets, our detection limits were similar to Kraus et al. (2011) at 20 au (∼15 M_J median mass limit), but a factor of 10 deeper in mass at 150 au (∼3 M_J median mass limit). Our probabilities of planet detection as a function of mass and semimajor axis are broadly comparable to the result from SHINE, the SPHERE infrared survey (Vigan et al. 2020) that used a larger sample of targets.

The continued lack of new brown dwarf companions at wide separations is further evidence of the so-called brown dwarf desert described by Marcy & Butler (2000) and Grether & Lineweaver (2006) extending to separations beyond that probed by radial velocity surveys. We were able to detect several known wide companions, including the roughly planetary-mass companion DH Tau b and the circumstellar disc around the companion to HK Tau.

We determined that, if the HR 8799 planets were placed in the TMC at the appropriate age, we could have detected analogues to HR 8799 b, c, and d around more than 15 per cent of our targets at an age of 1 Myr. Assuming a similar power law to Fernandes et al. (2019), we find that planets with the mass or semimajor axis of HR 8799 b, c, and d occur around less than 20 per cent of stars. Generalizing this to planets from 2–13 M_J at separations 10–500 au, we found that, assuming the same power law, the planet frequency in this mass and semimajor axis range is less than 30 per cent at a 90 per cent confidence level. Future instruments such as VIKiNG on VLTI and METIS on the E-ELT will be required to improve on our detection limits, to more precisely constrain planet frequency.

ACKNOWLEDGEMENTS

We thank the anonymous referee for their useful comments which greatly improved this study.

The data presented herein were obtained at the W. M. Keck Observatory, which is operated as a scientific partnership among the California Institute of Technology, the University of California, and the National Aeronautics and Space Administration. The observatory was made possible by the generous financial support of the W. M. Keck Foundation.

ALW would like to thank the Australian Government for their support through the Australian Postgraduate Award Scholarship and the Research School of Astronomy and Astrophysics at the Australian National University for the ANU Supplementary PhD Scholarship.

MJI acknowledges funding provided by the Australian Research Council (Discovery Project DP170102233 and Future Fellowship FT130100235).

CF acknowledges funding provided by the Australian Research Council (Discovery Project DP170100603 and Future Fellowship FT180100495), and the Australia-Germany Joint Research Cooperation Scheme (UA-DAAD).

DATA AVAILABILITY

The data underlying this article are available from the corresponding author on reasonable request.

REFERENCES

ALMA Partnership, 2015, ApJ, 808, L3
Andrews S. M., Williams J. P., 2005, ApJ, 631, 1134
Andrews S. M., Rosenfeld K. A., Kraus A. L., Wilner D. J., 2013, ApJ, 771, 129
Baraffe I., Chabrier G., Allard F., Hauschildt P., 2003, in Martin E., ed., Proc. IAU Symp. 211, Brown Dwarfs. Kluwer, Dordrecht, p. 41
Baraffe I., Homeier D., Allard F., Chabrier G., 2015, A&A, 577, A42
Berardo D., Cumming A., Marleau G.-D., 2017, ApJ, 834, 149
Bowler B. P., Nielsen E. L., 2018, Occurrence Rates from Direct Imaging Surveys, Handbook of Exoplanets. Springer, Cham, p. 155
Brogan C. et al., 2015, ApJ, 808, L3
Carpenter J. M., Ricci L., Isella A., 2014, ApJ, 787, 42
Crida A., Morbidelli A., 2007, MNRAS, 377, 1324
Cumming A., Butler R. P., Marcy G. W., Vogt S. S., Wright J. T., Fischer D. A., 2008, PASP, 120, 531
Fernandes R. B., Mulders G. D., Pascucci I., Mordasini C., Emsenhuber A., 2019, ApJ, 874, 81
Fitzpatrick E., Massa D., 2007, ApJ, 663, 320
Foreman-Mackey D., 2016, J. Open Source Softw., 1, 24
Foreman-Mackey D., Hogg D. W., Lang D., Goodman J., 2013, PASP, 125, 306
Ghez A., White R. J., Simon M., 1997, ApJ, 490, 353
Grether D., Lineweaver C. H., 2006, ApJ, 640, 1051
Güdel M. et al., 2007, A&A, 468, 353
Herczeg G. J., Hillenbrand L. A., 2014, ApJ, 786, 97
Huang J. et al., 2020, ApJ, 891, 48
Hunziker S., Quanz S. P., Amara A., Meyer M. R., 2018, A&A, 611, A23
Ireland M. J., 2013, MNRAS, 433, 1718
Itoh Y. et al., 2005, ApJ, 620, 984
Johns-Krull C. M. et al., 2016, ApJ, 826, 206
Kammerer J., Ireland M. J., Martinache F., Girard J. H., 2019, MNRAS, 486, 639
Keppler M. et al., 2018, A&A, 617, A44
Kraus A. L., Ireland M. J., 2011, ApJ, 745, 5
Kraus A. L., Ireland M. J., Martinache F., Hillenbrand L. A., 2011, ApJ, 731, 8
Kraus A. L., Ireland M. J., Cieza L. A., Hinkley S., Dupuy T. J., Bowler B. P., Liu M. C., 2013, ApJ, 781, 20
Kuruwita R. L., Ireland M., Rizzuto A., Bento J., Federrath C., 2018, MNRAS, 480, 5099
Lagrange A.-M. et al., 2010, Science, 329, 57
Long F. et al., 2018, ApJ, 869, 17
Marcy G. W., Butler R. P., 2000, PASP, 112, 137
Marleau G.-D., Cumming A., 2014, MNRAS, 437, 1378
Marleau G.-D., Mordasini C., Kuiper R., 2019, ApJ, 881, 144
Marley M. S., Fortney J. J., Hubickyj O., Bodenheimer P., Lissauer J. J., 2007, ApJ, 655, 541
Marois C., Macintosh B., Barman T., Zuckerman B., Song I., Patience J., Lafrenière D., Doyon R., 2008, Science, 322, 1348
Martinache F., 2010, ApJ, 724, 464
Mathieu R. D., Stassun K., Basri G., Jensen E. L. N., Johns-Krull C. M., Valenti J. A., Hartmann L. W., 1997, AJ, 113, 1841
Meshkat T., Kenworthy M. A., Quanz S. P., Amara A., 2013, ApJ, 780, 17
Metchev S. A., Hillenbrand L. A., 2009, ApJS, 181, 62
Mordasini C., 2013, A&A, 558, A113
Pope B., Tuthill P., Hinkley S., Ireland M. J., Greenbaum A., Latyshev A., Monnier J. D., Martinache F., 2016, MNRAS, 455, 1647
Prato L., Simon M., Mazeh T., Zucker S., McLean I. S., 2002, ApJ, 579, L99
Schlafly E. et al., 2014, ApJ, 789, 15
Soummer R., Pueyo L., Larkin J., 2012, ApJ, 755, L28
Spiegel D. S., Burrows A., 2012, ApJ, 745, 174
Stapelfeldt K. R., Krist J. E., Ménard F., Bouvier J., Padgett D. L., Burrows C. J., 1998, ApJ, 502, L65
Tanner A. et al., 2007, PASP, 119, 747
Thalmann C. et al., 2015, ApJ, 808, L41
Torres R. M., Loinard L., Mioduszewski A. J., Rodríguez L. F., 2009, ApJ, 698, 242
Van Der Plas G. et al., 2016, ApJ, 819, 102
Vigan A. et al., 2012, A&A, 544, A9
Vigan A., Fontanive C., Meyer M., Biller B., Bonavita M., Feldt M., 2020, A&A, Available at: https://doi.org/10.1051/0004-6361/202038107
Wallace A., Ireland M., 2019, MNRAS, 490, 502
Zhu Z., 2015, ApJ, 799, 16

This paper has been typeset from a TEX/LATEX file prepared by the author.